



# Unveiling the role of trivalent cation incorporation in Li-rich Mn-based layered cathode materials for low-cost lithium-ion batteries

Moustafa M. S. Sanad<sup>1</sup> · Arafat Toghan<sup>2,3</sup>

Received: 4 July 2021 / Accepted: 26 August 2021 / Published online: 3 September 2021  
© The Author(s), under exclusive licence to Springer-Verlag GmbH, DE part of Springer Nature 2021

## Abstract

A simple solvothermal route was successfully implemented for fabrication of Li-rich Mn-based layered cathode  $\text{Li}_{1.15}\text{Ni}_{0.15}\text{Co}_{0.15}\text{Mn}_{0.7}\text{M}_{0.01}\text{O}_2$  (LMLC) materials through incorporation of different trivalent cations ( $\text{M}^{3+}$ :  $\text{Al}^{3+}$ ,  $\text{Cr}^{3+}$  or  $\text{Fe}^{3+}$ ). The structural properties of mixed solid solution of rhombohedral  $\text{LiNiO}_2$  phase and monoclinic  $\text{Li}_2\text{MnO}_3$  phases were checked by X-ray diffraction (XRD) and X-ray photoelectron spectroscopy (XPS). LMLC-Fe sample shows the highest coercivity  $H_c$  value of about 198.1 Oe, and the lowest dielectric constant  $\epsilon_r$  about 74. LMLC-Cr sample exhibits the lowest activation energy ( $E_a = 0.163$  eV) for electric conduction as a result of the smallest cell volume and particle size. LMLC-Al electrode material delivers the highest initial charge and discharge capacity of about 140 and 104 mAh/g at 0.1 C, respectively maintaining around 70% of the initial capacity at 0.1C. Both LMLC-Al and LMLC-Cr samples show better high rate capabilities than that of LMLC-Fe sample.

**Keywords** Layered materials · Structural properties · Electronic conductivity · Lithium-ion batteries

## 1 Introduction

The accelerated development of electric vehicles (EVs) and hybrid electric vehicles (HEVs) as well as the installation of huge renewable energy power plants has enforced the need to high energy density batteries mainly lithium-ion batteries [1, 2]. Considering that, the Li-rich layered cathode materials have been extensively investigated and attracted higher attention than the conventional cathodes made of  $\text{LiCoO}_2$ ,  $\text{LiMn}_2\text{O}_4$  and  $\text{LiFePO}_4$  owing to their high storage capacities [3–5]. During the last few years, the electrochemical performance of Li-rich Mn-based layered cathode (LMLC) materials  $x\text{Li}_2\text{MnO}_3-(1-x)\text{LiNiO}_2$  has clearly surpassed that of commercial Ni-rich layered cathodes materials (NMC) [6–8]. The reason for their

preference for next generation of EVs can be attributed to the enhanced structural and thermal stability as a result of the presence of inactive  $\text{Li}_2\text{MnO}_3$ , delivering large charge-discharge capacities and its lower cost and toxicity [9–11]. However, the solid solution system of LMLC materials still suffers from some operational problems such as low initial coulombic efficiency or low electric conductivity leading to a poor rate capability [12–14]. Huge efforts have been made to overcome all the aforementioned practical difficulties through several strategies such as surface modifications [15, 16], doping with transition metals ions [17, 18] and controlling the morphology of particles [19, 20]. Apparently, previous research studies demonstrated that the bulk doping with cations like  $\text{Mg}^{2+}$  [21],  $\text{Cr}^{3+}$  [22],  $\text{Zr}^{4+}$  [23],  $\text{Al}^{3+}$  [24],  $\text{Mo}^{4+/6+}$  [19],  $\text{V}^{4+/5+}$  [25],  $\text{Ti}^{4+}$  [26],  $\text{Fe}^{3+}$  [27] or  $\text{Sn}^{4+}$  [28] would stabilize the layered material superstructure and significantly hinder the spinel phase transformation upon cycling [29–31]. In addition, various preparation wet chemical methods, e.g. co-precipitation [32], sol-gel [33] and solvothermal [34], have been employed to prepare different morphologies of LMLC materials in the nanosized scale to boost the lithium ions diffusion rate and hence improving the storage capacity and coulombic efficiency as well. In this view, the effect of incorporation of a small proportion of trivalent

✉ Moustafa M. S. Sanad  
mustafa\_sanad2002@yahoo.com

<sup>1</sup> Central Metallurgical Research and Development Institute, P.O. Box: 87, Helwan, Cairo, Egypt

<sup>2</sup> Chemistry Department, Faculty of Science, South Valley University, Qena 83523, Egypt

<sup>3</sup> Chemistry Department, College of Science, Imam Mohammad Ibn Saud Islamic University (IMSIU), Riyadh 11623, Saudi Arabia

metal ions (~ 1%) on the structural, morphological and electrochemical performance of LMLC materials was explored as principal objective of this work. Thus, three samples of  $\text{Li}_{1.15}\text{Ni}_{0.15}\text{Co}_{0.15}\text{Mn}_{0.7}\text{M}_{0.01}\text{O}_2$  materials doped with 1wt% of  $\text{Al}^{3+}$ ,  $\text{Cr}^{3+}$  and  $\text{Fe}^{3+}$  trivalent cations were synthesized via solvothermal technology. The fabricated electrodes from these materials were investigated by cyclic voltammetry and electrochemical impedance spectroscopy to clarify the reaction mechanism. The charge/discharge experiments were also conducted by applying different C-rates as well as long-term stability tests.

## 2 Experimental

### 2.1 Synthesis of layered metal oxides

A single phase of Li-rich and Mn-based layered and subsequently doped by trivalent metal-ion  $\text{Li}_{1.15}\text{Ni}_{0.15}\text{Co}_{0.15}\text{Mn}_{0.7}\text{M}_{0.01}\text{O}_2$  nanoparticles, where M:  $\text{Al}^{3+}$ ,  $\text{Cr}^{3+}$  or  $\text{Fe}^{3+}$  ions were prepared via simple solvothermal route. A mixture of ethylene glycol (density = 1.11 g/cm<sup>3</sup>) and absolute ethanol (1:1, by volume) serves as organic solvent. The three M-doped samples  $\text{Li}_{1.15}\text{Ni}_{0.15}\text{Co}_{0.15}\text{Mn}_{0.7}\text{Al}_{0.01}\text{O}_2$  (LMLC-Al),  $\text{Li}_{1.15}\text{Ni}_{0.15}\text{Co}_{0.15}\text{Mn}_{0.7}\text{Cr}_{0.01}\text{O}_2$  (LMLC-Cr) and  $\text{Li}_{1.15}\text{Ni}_{0.15}\text{Co}_{0.15}\text{Mn}_{0.7}\text{Fe}_{0.01}\text{O}_2$  (LMLC-Fe) were prepared by adding stoichiometric amounts of lithium nitrate trihydrate  $\text{LiNO}_3 \cdot 3\text{H}_2\text{O}$  (99.9%, 1.4 g), nickel (II) acetate tetrahydrate  $\text{Ni}(\text{CH}_3\text{CO}_2)_2 \cdot 4\text{H}_2\text{O}$ , (99.9%, 0.75 g), manganese acetate tetrahydrate  $\text{Mn}(\text{CH}_3\text{CO}_2)_2 \cdot 4\text{H}_2\text{O}$  (99.9%, 3.43 g), cobalt acetate tetrahydrate  $\text{Co}(\text{CH}_3\text{CO}_2)_2 \cdot 4\text{H}_2\text{O}$  (99%, 0.75 g) and either  $\text{Al}(\text{NO}_3)_3 \cdot 9\text{H}_2\text{O}$  (99.9%, 0.078 g) or chromium (III) nitrate nonahydrate  $\text{Cr}(\text{NO}_3)_3 \cdot 9\text{H}_2\text{O}$  (99.9%, 0.08 g) or iron (III) nitrate nonahydrate  $\text{Fe}(\text{NO}_3)_3 \cdot 9\text{H}_2\text{O}$  (99.9%, 0.08 g) to 120 ml of the solvent mixture. Afterwards the salts were completely dissolved and the molar ratio of Li:Ni:Co:Mn:M<sup>3+</sup> was 1.15:0.15:0.15:0.7: 0.01. The pH of the three mixtures was adjusted to 9.7 using an ammonium hydroxide solution (33%) to form the corresponding hydroxides. The formed suspensions were stirred for 15 min to achieve higher homogeneity. This new homogeneous mixture was then transferred into a closed Teflon container. The container was heated up to 180 °C (4.5 bar), and afterwards the temperature was hold for 12 h. Subsequently, the obtained solvothermal precursor solutions/suspensions were boiled at 105 °C under ambient pressure to evaporate the organic solvents. Each dried precursor was then pre-calcined at 500 °C (4 h) in air. The pre-calcined powders were finally calcined at 800 °C (3 h) in air and subsequently quenched at open air conditions. Finally, the as-prepared powders were intensely ground and subjected to further characterizations.

### 2.2 Characterizations

Bruker AXS diffractometer (D8-ADVANCE) with Cu K $\alpha$  radiation ( $\lambda = 1.5406 \text{ \AA}$ ) operating at 40 kV and 10 mA was utilized to record X-ray powder diffraction (XRD) pattern. The diffraction scan was done between  $2\theta$  range 10°–80° with a rate of about 0.5° min<sup>-1</sup>. The XPS spectra for the LMLC-Al sample were measured using X-ray photoelectron spectrometer (Thermo Scientific, Model: K-Alpha surface analysis) equipped with monochromatic small-spot XPS system to scan spectra in the range of 0–1000 eV using X-ray source–Al K $\alpha$  source ( $\lambda = 8.339 \text{ \AA}$ ) and calibrated by C 1 s line. The surface morphology and particle size of the as-prepared nanopowders were examined by field emission scanning electron microscope (FE-SEM) using the model QUANTA FEG250 from Genesis, Holland. The elemental analysis was performed with built-in unit for energy-dispersive X-ray spectroscopy analysis (EDS). The morphology of the cathode materials was identified by high-resolution transmission electron microscopy (HR-TEM) with a TECNAI G2 S-Twin microscope operating at 200 kV. The magnetization characteristics of all samples were measured at room temperature using a vibrating sample magnetometer (7400–1 VSM, U.S. Lake Shore Co., Ltd., USA) at maximum applied field 20 kOe. A thin-film layer of silver suspension ink was coated on the sintered pellet sides, in order to serve as electrodes for the dielectric measurements. Dielectric and ac conductivity measurements were determined in the temperature range of 300–525 K at 10 kHz using a Stanford Research RCL Bridge (Model: SR-720). The voltage bias: 2 VDC (internal) and 0–40 VDC (external).

### 2.3 Battery assembly and electrochemical testing

All processing steps for the as-synthesized positive electrode materials have been carried out in Argon filled glove box. The electrode slurry was prepared by mixing each active material (LMLC-Al, LMLC-Cr or LMLC-Fe) with carbon black (Super P C 65, Imerys) as conducting additive and polyvinylidene fluoride (PVDF, Solef 5130, Solvay Solexis) as binder in mass ratio NCM/CB/PVDF 83/10/7 in *N*-methyl pyrrolidone (NMP). The formed homogeneous slurry was coated on Al-foil as current collector and the as-prepared electrodes were dried under vacuum at 90 °C for (8 h). The cathode material loading is 4 mg/cm<sup>2</sup>. Finally, circular electrodes with a diameter of 12 mm were laser-cut and dried at 90 °C for 24 h under vacuum. At least three-electrode cells (Swagelok®) with Li as reference and counter electrode were assembled with each of the as-prepared electrodes. Freudenberg FS 2190

served as separator. A commercial carbonate mixture EC/DMC (1:1) (Sigma-Aldrich) with 1 M  $\text{LiPF}_6$  conducting salt was utilized as electrolyte. The rate capability tests and the long-term cycling were carried out between 3.0 and 4.8 V versus  $\text{Li/Li}^+$  with the charge/discharge procedure showed in Table S1 “Supplementary file” by means of a Maccor 4200 battery tester. Cyclic voltammetry measurements were performed in three-electrode cells as well in the voltage range of 3.0–4.8 V (vs.  $\text{Li}^+/\text{Li}$ ) at scan rate of  $10 \mu\text{Vs}^{-1}$  by means of a BioLogic VSP Potentiostat.

### 3 Results and discussion

#### 3.1 Structural properties

The as-prepared layered samples (LMLC-Al, LMLC-Cr or LMLC-Fe) exhibit the same diffraction patterns as shown in Fig. 1. The XRD results of each composition indicate the presence of superstructure composed of two different phases, Rhombohedral phase is appeared as the main phase, and its peak signatures are matching to the common  $\text{LiNiO}_2$  layered structure with R-3 m space group (JCPDS card no. 96-0063) [35]. The other minor peaks correspond to the monoclinic  $\text{Li}_2\text{MnO}_3$  phase with C2/m space group (JCPDS card no. 84-1634) [36]. The crystallographic parameters are calculated using the integrated software analysis (Topas 4.1)

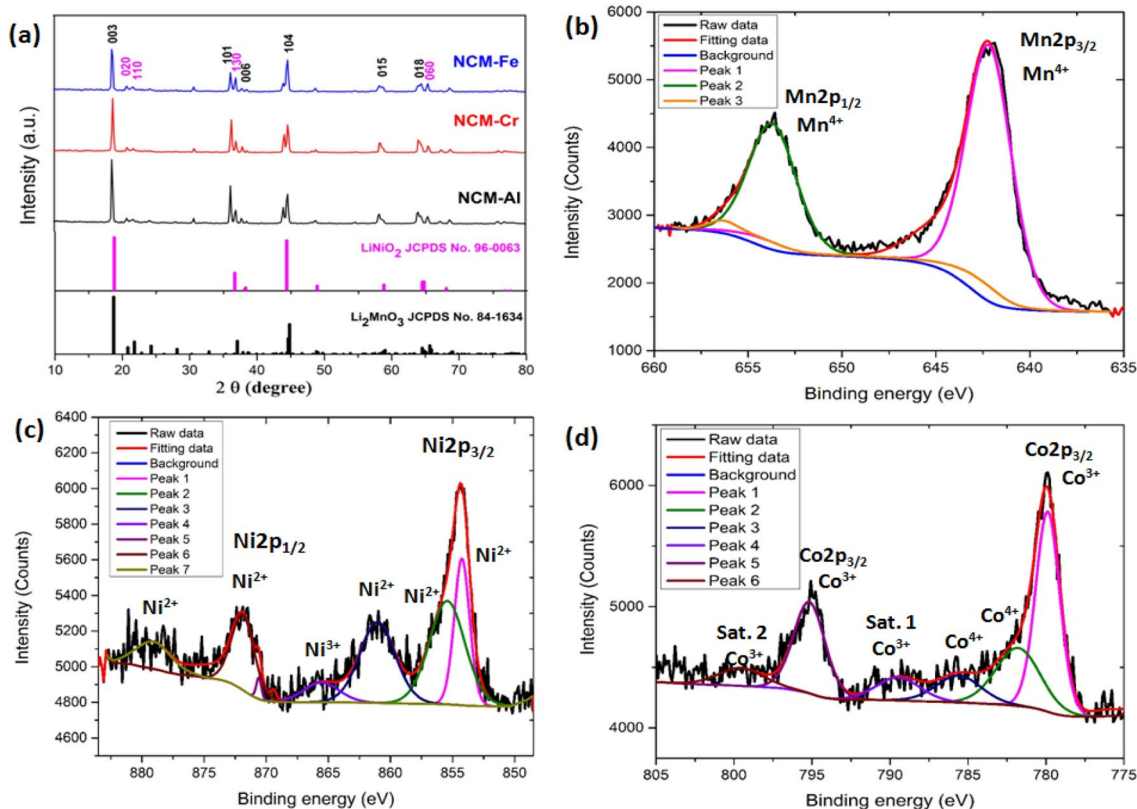


**Fig. 1** XRD patterns of  $\text{Li}_{1.15}\text{Ni}_{0.15}\text{Co}_{0.15}\text{Mn}_{0.7}\text{Al}_{0.01}\text{O}_{2+\delta}$  layered samples calcined at  $800^\circ\text{C}$  for 3 h using different cations (a). XPS spectra of Mn 2P (b), Ni 2P (c) and Co 2P (d)

**Table 1** Crystallographic parameters of layered samples prepared via solvothermal method annealed at  $800^\circ\text{C}$  for 3

Sample	Crystallite size (nm)	$a$ (Å) ( $\pm 0.005$ )	$c$ (Å) ( $\pm 0.004$ )	$c/a$ (Å)	$V$ (Å <sup>3</sup> )	$I_{(003)}/I_{(104)}$
LMLC-Al	120	2.879	14.196	4.931	117.666	2.15
LMLC-Cr	74	2.864	14.122	4.931	115.836	1.94
LMLC-Fe	102	2.879	14.195	4.931	117.657	1.34

and listed in Table 1. The crystallite size ( $D$ ) was calculated using the common Scherrer equation  $D = k\lambda/\beta\cos\theta$ , where  $k$  is the Scherrer constant ( $k = 0.89$ ),  $\lambda$  is the X-ray wavelength,  $\beta$  is the peak width at half maximum, and  $\theta$  is the Bragg's diffraction angle. The higher the intensity ratio between the two reflections (003) and (104) than 1.2, the higher is the cation mixing in the layered LMO<sub>2</sub> material. Meanwhile, if the  $I_{(003)}/I_{(104)}$  ratio is below 1.2, a weak bonding of transition elements with Li atoms in the crystal structure is caused [37, 38]. Obviously, the three layered samples exhibited higher values of  $I_{(003)}/I_{(104)}$  ratio above 1.2 and LMLC-Al electrode material showed the highest value of about 2.15, which suggest high degree of transition elements occupation inside the Li-O layers. Moreover, the appearance of well separated peaks corresponding to (101) and (006) planes indicates the formation of the well crystalline layered Li<sub>2</sub>MnO<sub>3</sub> structure of (Li[Li<sub>1/3</sub>Mn<sub>2/3</sub>]O<sub>2</sub>) type. Basically, the combination of these two different crystal structures could be possible at the atomic level as the close packed layers have similar interlayer spacing; thus their integration on molecular level is deeply observed in the present case [39, 40]. Accordingly, a successful formation of complex structure was achieved by the proposed solvothermal technique. The calculated average crystallite sizes are about 120, 74 and 102 nm for Al-, Cr- and Fe-doped LMLC layered structures, respectively. Thus, the significant decrease in the crystallinity of LMLC-Cr and LMLC-Fe could be attributed to the decrease in the crystallinity and crystallite size. It is indicated that LMLC-Al has the maximum cell volume, while the Cr-doped LMLC samples possessed the smallest unit cell volume. The reason for increasing the cell volume of LMLC-Al > LMLC-Cr > LMLC-Fe because atomic mass of Al (27 u) is lower than Cr (52 u) and Fe (56 u), thus the number of doped atoms of Al is higher than Cr and Fe leading to more octahedral centers which creates more inter spaces in the structure resulting in the lattice expansion along a and c axes for LMLC-Al and shrinkages in the lattice parameters a and c of LML-Cr. The influence of the trivalent doping cation on the oxidation state of Mn, Ni and Co can be investigated by applying the X-ray photoelectron spectroscopy (XPS) analysis for LMLC-Al sample as an example. Figure 1b reveals the two principle peaks of Mn2p<sub>3/2</sub> and Mn2p<sub>1/2</sub> at binding energies 642.2 and 653.7 eV, respectively. The separation between these two peaks is about 11.5 eV, which indicates the presence of Mn<sup>4+</sup> [41, 42]. In addition, the depth XPS scan of Ni 2p in Fig. 1c displays two strong peaks of Ni2p<sub>3/2</sub> at 854.3 eV and Ni2p<sub>1/2</sub> at 872.5 eV as a result of Ni<sup>2+</sup> cation existence. The other mild peaks observed at 856.5, 861.5 and 879 eV provide an additional confirmation for the presence of Ni<sup>2+</sup> cations [43, 44]. The observation of the weak peak at 866 eV signifies the presence of Ni<sup>3+</sup> traces (about 0.5%), which results from the valence degeneracy between Mn<sup>4+</sup> and Ni<sup>2+</sup> cations through the reversible reaction:

$\text{Mn}^{4+} + \text{Ni}^{2+} \leftrightarrow \text{Ni}^{3+} + \text{Mn}^{3+}$  [45, 46] or due to the effect of Al<sup>3+</sup> doping. Figure 1d illustrates the Co2p XPS spectra, which shows two main peaks of Co2p<sub>3/2</sub> and Co2p<sub>1/2</sub> at binding energies about 780 and 795.2 eV, respectively. The observed splitting distance between these two peaks of about 15.2 eV confirms the existence of Co<sup>3+</sup> cations [47, 48]. Moreover, the detection of two satellite peaks around 790 and 802 eV gives strong evidence also for Co<sup>3+</sup> cations formation [48, 49].

## 3.2 Surface morphology

### 3.2.1 Scanning electron microscope

The microstructure of the three powders is shown in Fig. 2a–e at two different magnifications: 10000X and 30000X. The LMLC samples are homogenous and highly dispersed and exhibit both rhombohedral (or trigonal bipyramids) and monoclinic morphologies as detected by the XRD measurements. The average particle sizes are (500–1000 nm), (300–500 nm) and (300–700 nm) for Al-, Cr- and Fe-doped samples, respectively. The observed sharp edges in each regular particle geometry confirm the successful incorporation of doping metal ions without crystal lattice destruction and reflects the crystallinity improvement as well. It is worth to mention that the pores and path depths created between both types of crystal morphologies in each sample demonstrate good electronic paths for Li ions during charge/discharge processes.

The EDS analysis of LMLC electrode materials confirmed the incorporation of trivalent cations (Al<sup>3+</sup>, Cr<sup>3+</sup>, Fe<sup>3+</sup>). It is noticed that Fe<sup>3+</sup> cation is found to be actually doped in the LMLC with higher stoichiometric amount (1.66%) than the intended percentage (1%). Meanwhile, both Al<sup>3+</sup> and Cr<sup>3+</sup> cations are found to be existed in the LMLC structure with lower percentages 0.42% and 0.68% than the intended one. The elemental analysis of other elements Mn, Ni, Co and O in all the three LMLC samples are quite different. The reason for this divergence could be attributed to the difference in the area exposed to the electron beam and the thickness of each powder LMLC sample mounted on the carbon tape could affect on the accuracy of EDS results (Fig. 3).

### 3.2.2 Transmission electron microscope

TEM/HR-TEM images with different magnifications for LMLC crystals, lattice pattern and selected area electron diffraction patterns (SAED) can be observed in Fig. 4a–i. The normal TEM images, Fig. 4a, b and c, of both LMLC-Al (a) and LMLC-Cr (b, c) materials exhibit well crystalline nanoplates of rectangular-like shape with different side dimensions, about 350–400 nm length, 250–280 nm width

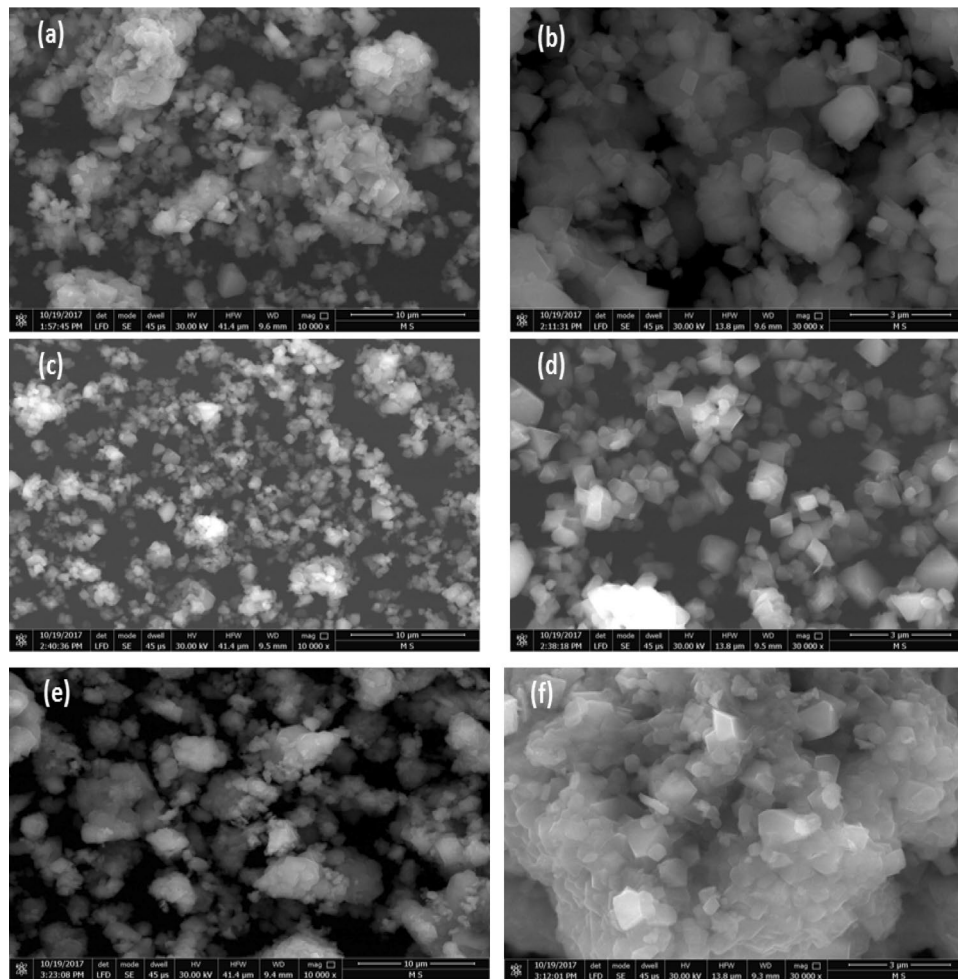


**Fig. 2** FEG-SEM micrographs of  $\text{Li}_{1.15}\text{Ni}_{0.15}\text{Co}_{0.15}\text{Mn}_{0.7}\text{M}_{0.01}\text{O}_{2+\sigma}$  calcined at  $800\text{ }^{\circ}\text{C}$  for 3 h: (a, b) LMLC-Al, (c, d) LMLC-Cr and (e, f) LMLC-Fe. (Magnification: a, c, e:  $10\text{ }\mu\text{m}$ ; b, d, f:  $3\text{ }\mu\text{m}$ )

and 15–30 nm thickness. Alongside to this, the LMLC-Al particles have larger size than that of LMLC-Cr particles suggesting a good agreement with XRD and SEM results. Actually, the rhombohedral  $\text{LiMO}_2$  and monoclinic  $\text{Li}_2\text{MnO}_3$  phases of the LMLC-Fe sample can be easily distinguished from HRTEM images and SAED patterns, as depicted in Fig. 4d, e, f, h.

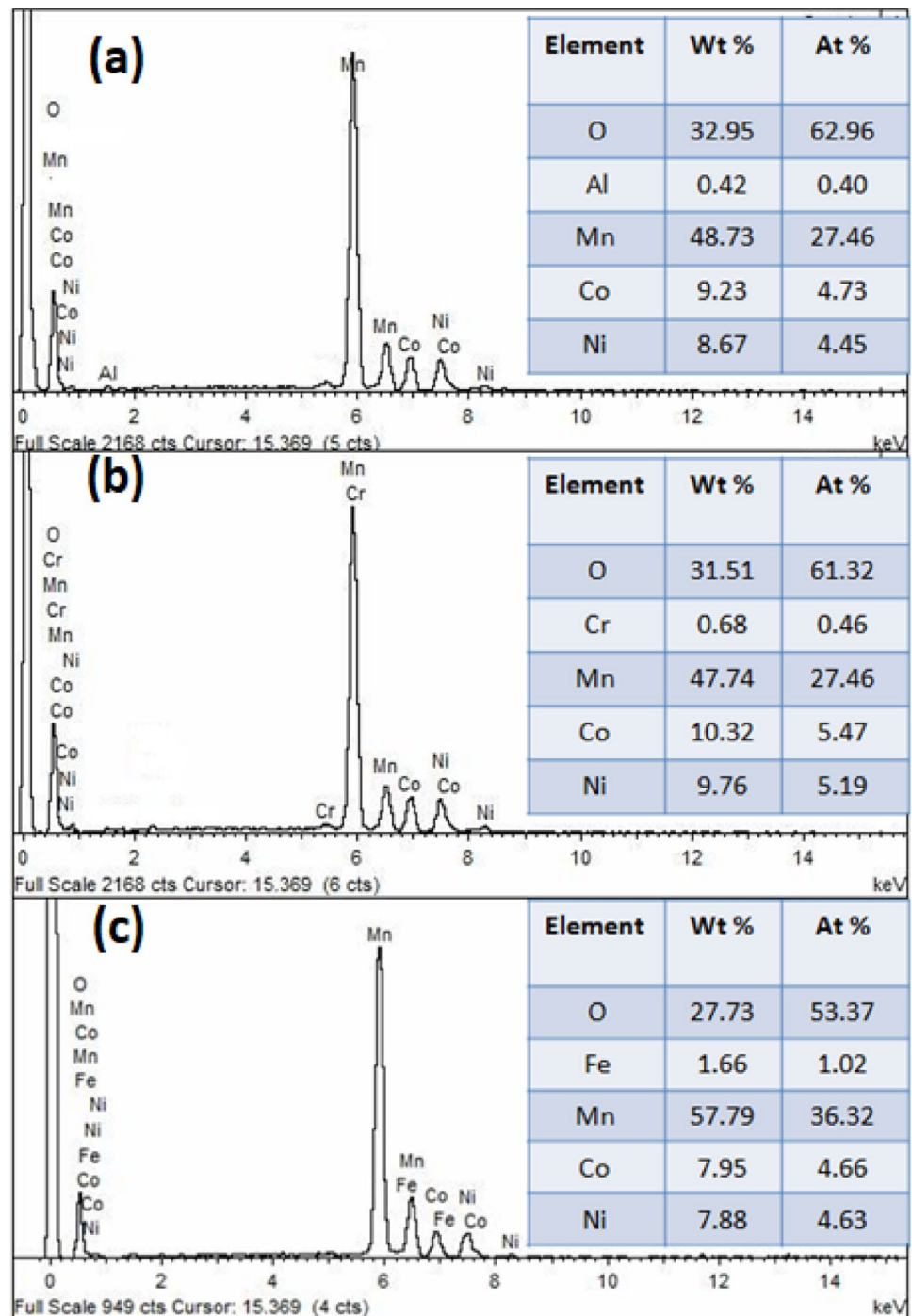
Figure 4d reveals the HR-TEM image for the LMLC-Fe nanocrystals which indicates the existence of two  $d$ -spacing distances 0.2 and 0.47 nm corresponding to the indexed planes (104) and (0 0 3) planes, respectively, of  $\text{LiMO}_2$  lattice pattern [50, 51]. Figure 4e f shows the HR-TEM analysis for another spot in LMLC-Fe nanoparticles with lattice fringes of  $\text{Li}_2\text{MnO}_3$  ( $d_{020}=0.43\text{ nm}$ ) calculated by the built-in Fast Fourier Transformation (FFT) software. Thus, the corresponding miller indices of the FFT of LMLC-Fe composite structure are illustrated in Fig. 4g. Moreover, the observed and simulated electron diffraction pattern for the corresponding crystallographic orientations (Miller indices)

of LMLC-Fe nanoparticles is shown in Fig. 4h, i. The ring pattern is a common type of the diffraction pattern that explains the existed phases according to the  $d$ -spacing (the radius of each ring) and  $hkl$ . It is clear that the bright and intense rings in SAED are related to rhombohedral  $\text{LiMO}_2$  phase, while the small and less bright rings correspond to monoclinic  $\text{Li}_2\text{MnO}_3$  phase.

### 3.3 Magnetic and dielectric properties

As the movement of lithium ions and the transfer of electrons can take place simultaneously. Thus, applying the localized electrons model is highly preferred due to the fact that many cathode materials are poor conductors. Therefore, magnetic properties of the three LMLC samples were tested in order to investigate the change in the magnetic interactions within transition metal layers by doping with different trivalent cations which can lead to a change in the orbital overlapping ( $d$ - and  $-p$  orbitals) causing a change in the

**Fig. 3** EDS analysis of **a** LMLC-Al, **b** LMLC-Cr, **c** LMLC-Fe



ions mobility and electronic properties. Hence, prediction of electron transfer pathways and characteristics gives an indication about the electrochemical behavior of multivalent electrode materials.

The field-dependent magnetization measurements are conducted at room temperature to study the magnetic behavior of LMLC materials as shown in Fig. 5a and the corresponding data are represented in Table 2. Weak ferromagnetic behavior was clearly demonstrated

for the LMLC material. In particular, the magnitudes of saturation magnetization ( $M_s$ ) and remanence magnetization ( $M_r$ ) were decreased with increasing ionic radius of dopant ions  $\text{Fe}^{3+} > \text{Cr}^{3+} > \text{Al}^{3+}$ . However, the coercivity ( $H_c$ ) was significantly increased with increasing ionic radius of metal ions as well as decreasing average particle sizes and magnetocrystalline anisotropy. The obtained results showed good consistency with the previous reports of layered cathode materials [52, 53]. Furthermore, the

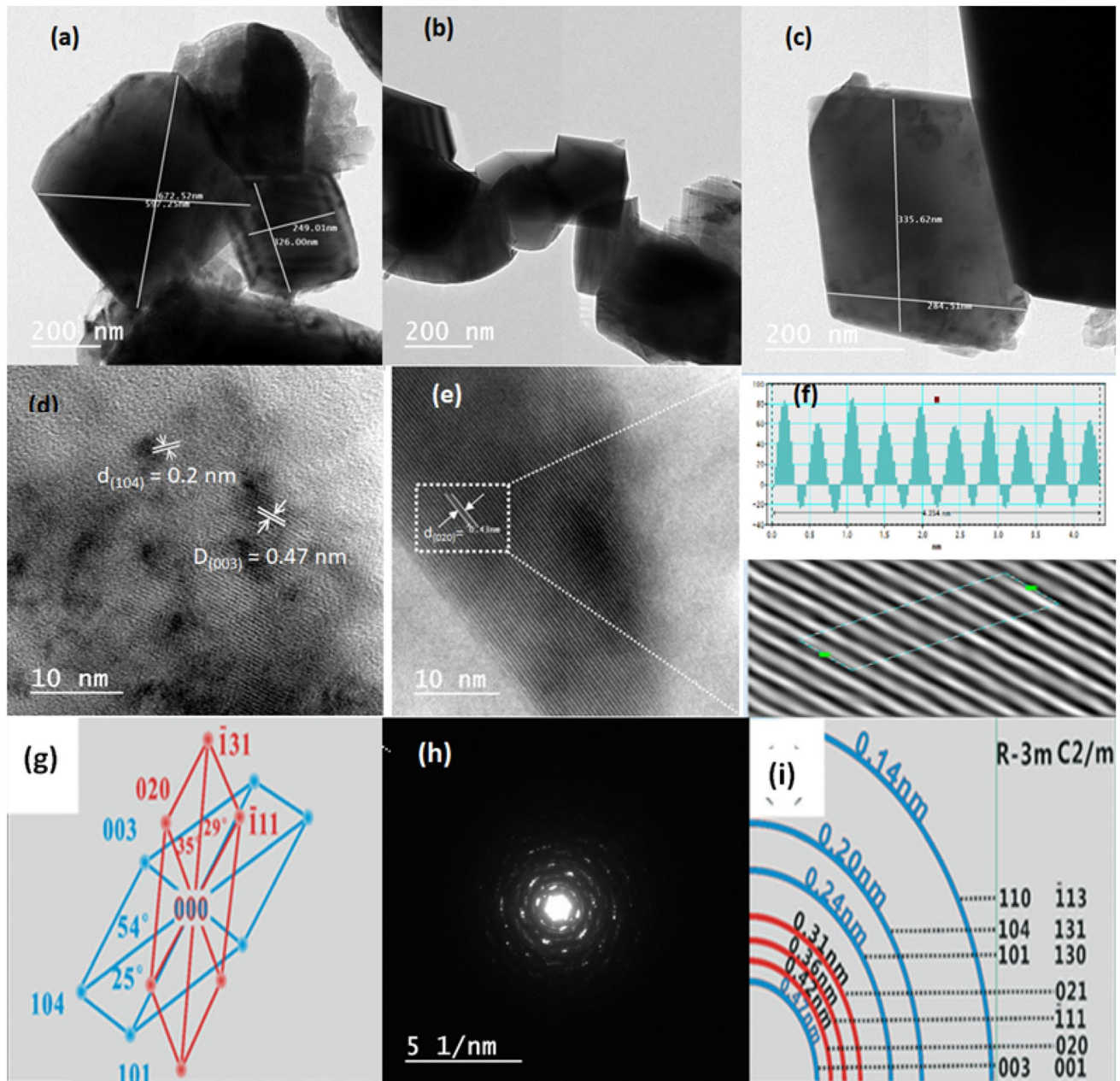


**Fig. 4** TEM images of Li and Mn rich layered samples calcined at 800 °C for 3 h: **a** LMLC-Al, **b**, **c** LMLC-Cr, HR-TEM images and d-spacings of R-3 m phase (**d**) and C2/m phase in LMLC-Fe nanocrystals (**e**). Fast Fourier Transformation (FFT) of lattice fringes of C2/m phase in LMLC-Fe nanocrystals (**f**). The corresponding

Miller indices of the FFT of LMLC-Fe composite structure. Observed and simulated electron diffraction pattern for the corresponding crystallographic orientations (Miller indices) of LMLC-Fe nanoparticles (**h**, **i**)

ground samples of layered phases were pressed and sintered in air at 830 °C to study the electrical properties of sintered LMLC materials. The electronic conductivity measurements are conducted at 10 kHz by using ac impedance spectroscopy technique to unveil the mobility of Li cations and electrons in the tunnels of layered framework structures as depicted in Fig. 5b, c. It is found that the dielectric constant of all samples strongly increases with

increasing temperature from 40 to 50 °C. This behavior directly changed to be decreased with further increase in the temperature reaching the steady state at 80 °C. Likely, the dielectric loss of all samples decreased with increasing the temperature from 50 to 90 °C and then start to increase up to 140 °C. It is obvious that the LMLC-Fe sample showed the lowest values of both dielectric loss ( $\tan \delta = 1.75$ ) and dielectric constant ( $\epsilon_r = 74$ ) at room

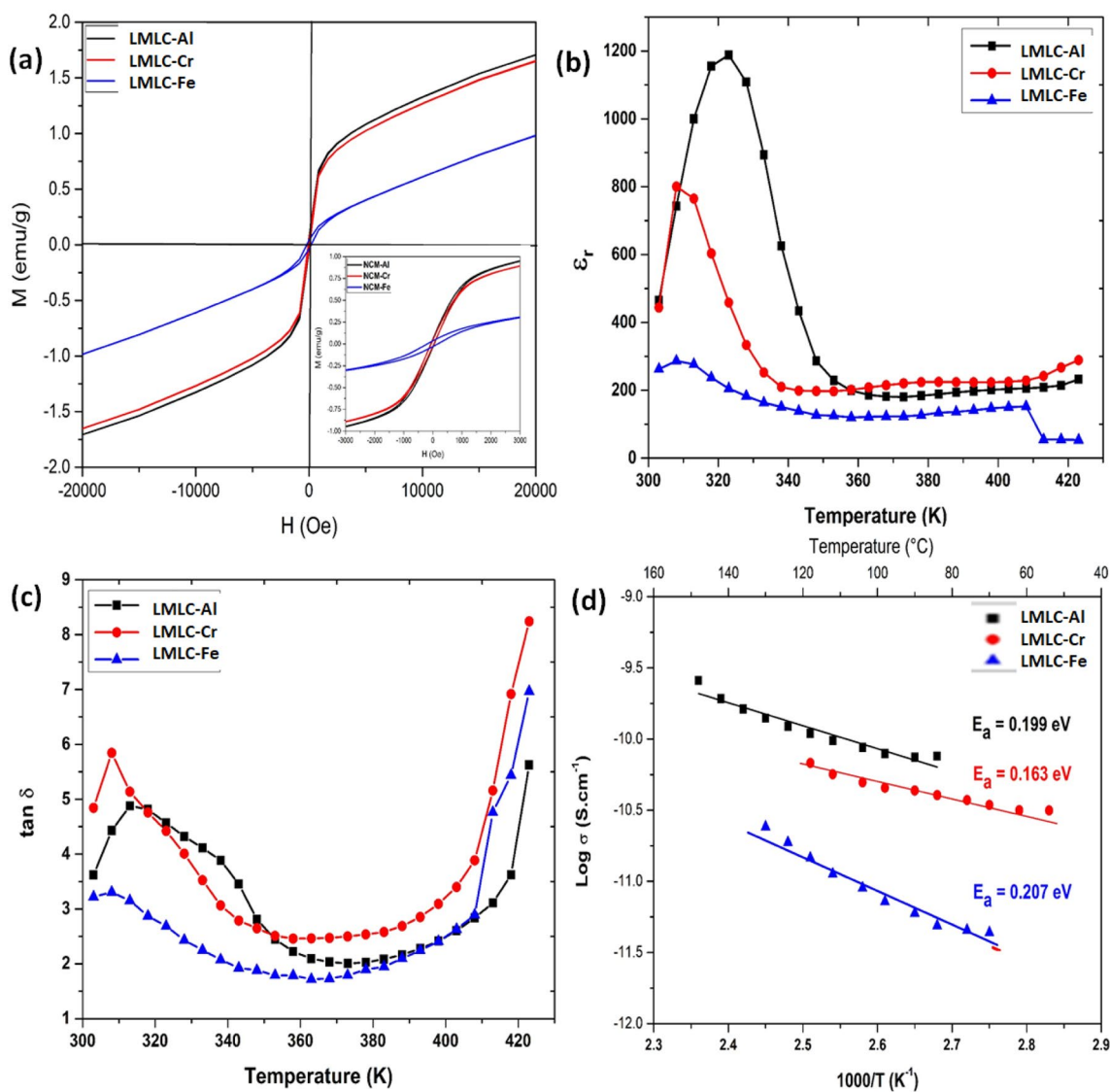


**Fig. 5** **a** M-H hysteresis loop of the as-prepared layered samples, **b** Variation of dielectric constant and absolute  $T$ , **c** Variation of dielectric loss and absolute  $T$ , and **d** Arrhenius plot of electrical conductivity versus reciprocal of absolute  $T$

**Table 2** Magnetic properties of layered samples prepared via solvothermal method annealed at 800 °C for 3 h

Sample	Magnetic properties			
	$M_s$ , emu/g	$M_r$ , emu/g $\times 10^{-3}$	$H_c$ , Oe	$M_r/M_s \times 10^{-3}$
LMLC-Al	1.71	65.74	76.58	38.51
LMLC-Cr	1.65	47.43	95.86	28.68
LMLC-Fe	0.98	40.82	198.10	41.48

temperature and the same dielectric behavior achieved with rising the temperature. In addition, the LMLC-Al sample possessed the maximum value of ( $\epsilon_r$ ) and ( $\tan \delta$ ) in the temperature range 30–70 °C, and shows moderate values above 70 °C. On the other hand, the common

**Table 3** Electrical and dielectric properties of the sintered pellets of layered samples at 10 kHz and 298 K

Samples	$\ln \sigma$ AC	$\tan \delta$	$\epsilon_r$	$E_a$ (eV)
LMLC-Al	-10.46	2.3	109	0.199
LMLC-Cr	-8.73	3.25	89	0.163
LMLC-Fe	-9.53	1.75	74	0.207

Arrhenius relation is implemented to calculate the required activation energy for electronic conduction in the bulk structure [54], as plotted in Fig. 5d. Generally, the electrical conductivity linearly increases with rising the temperature from 50 to 150 °C. Accordingly, the LMLC-Cr sample exhibited the lowest value of activation energy



( $E_a = 0.163$  eV) of conduction as a result of smallest cell volume and particle size as well. Meanwhile, LMLC-Fe sample revealed the highest value of activation energy of conduction ( $E_a = 0.207$  eV) over the temperature range (40–160 °C) which might be correlated to the less homogeneity in the layered structure and large cell volume. Table 3 summarizes the electrical and dielectric properties of the sintered pellets of layered LMLC samples at 10 kHz and 298 K. The measured LMCL samples showed similar

electrical and dielectric behavior to that of other layered cathode materials [55–57].

### 3.4 Electrochemical examination

#### 3.4.1 Galvanostatic cycling and cyclic voltammetry

The charge–discharge profiles at 0.2C rates for the first four cycles of LMLC-Al, LMLC-Cr and LMLC-Fe electrode

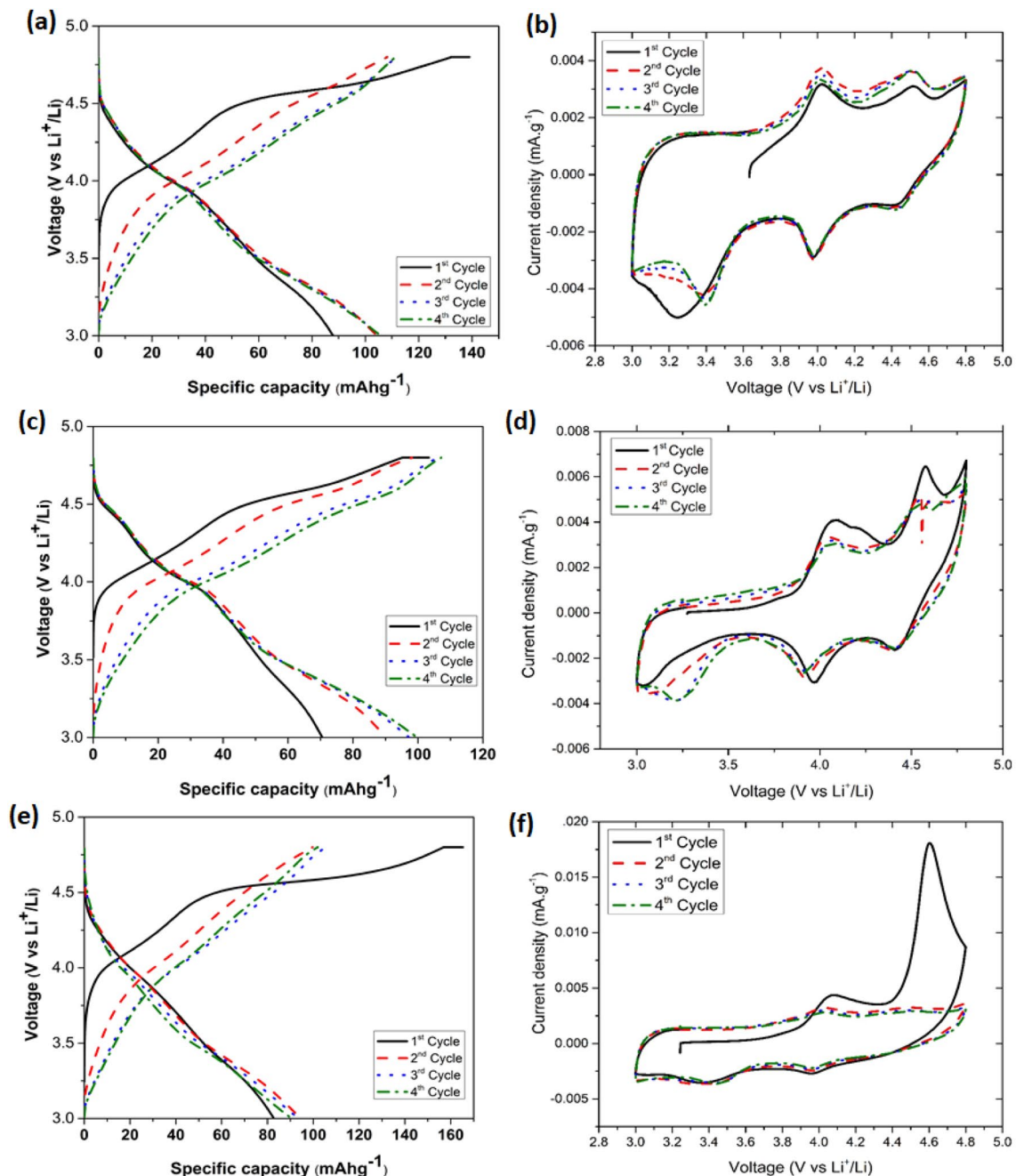


**Fig. 6** Galvanostatic charge–discharge profile for the formation cycle and subsequent three cycles vs.  $\text{Li}^+/\text{Li}$  at rate of 0.2C. The corresponding CVs for the first four charge–discharge processes at scan rate of  $10 \mu\text{V}\cdot\text{s}^{-1}$ : **a, b** LMLC-Al, **c,d** LMLC-Cr, and **e, f** LMLC-Fe, respectively

materials are depicted in Fig. 6a, c and e while the corresponding cyclic voltammograms (CV) of LMLC-Al, LMLC-Cr and LMLC-Fe are illustrated in Fig. 6b, d and f. It is found that the LMLC-Fe achieves the maximum initial charge capacity about 165 mAh/g at 1 C which correspond to 60% of the theoretical capacity. In contrast, LMLC-Cr achieves the maximum coulombic efficiency about 92.5% during the subsequent 4th cycle. The reason for this change can be significantly explained by the cyclic voltammetry and electrochemical impedance spectroscopy studies. As visible in Fig. 6b, d and f at the beginning of the first cycle, from open circuit potential up to 3.7 V, the Mn ions remain electrochemically inactive, however in the following cycles between 3.0 V and ca. 3.7 V, the oxidation of  $Mn^{3+}$  to  $Mn^{4+}$  takes place. This is visible by the broad current peaks from the second cycle and further in the CV of each material under study [58]. The  $Mn^{4+}$  to  $Mn^{3+}$  reduction occurs around 3.4 V.

For all three test samples, it can be noted that oxidation reactions of  $Ni^{2+}$  to  $Ni^{3+}$  and then to  $Ni^{4+}$  as well as  $Co^{3+}$  and  $Co^{4+}$  during charge are responsible for the first anodic peaks around 4.0 V [18]. On the cathodic side of the cyclic voltammogram, this is the reduction of  $Ni^{4+}$  to  $Ni^{2+}$  and

$Co^{4+}$  to  $Co^{3+}$ . The sharp peak during the first cycle around 4.6 V is only seen in the samples LMLC-Cr and LMLC-Fe due to irreversible electrochemical material activation reaction that decomposes  $Li_2MnO_3$  into  $Li_2O$  and  $MnO_2$  and yet oxygen is released. This irreversible reaction causes a crystal structure transformation of the cathode material according to the literature also. However, this occurrence has no negative influence on the electrochemical performance of the cathode, and it is very necessary for the further stable function of Li-rich cathode materials [59]. The peak is not present in the 2-nd, 3-rd and 4-th cycle for both materials. Generally, the subsequent cycles overlap each other, which is an evidence for a very good electrochemical reversibility of the as-presented layered cathode materials.

### 3.4.2 Electrochemical impedance spectroscopy (EIS)

Figure 7a, b illustrates the Nyquist plots for the assembled LMLC batteries before and after galvanostatic cycling at 0.2 C. In addition, the measured EIS parameters after fitting of the obtained Nyquist plots for all cells are listed in Table 4. It is revealed that LMLC-Al cell demonstrates the lowest values for ohmic resistance ( $R_s$ ), while the LMLC-Cr

**Fig. 7** Nyquist plots for the LMLC-Al, LMLC-Cr or LMLC-Fe cells at 0.2C rate before cycling (a), and after 10 cycles (b). EIS equivalent circuit of each cell (c)

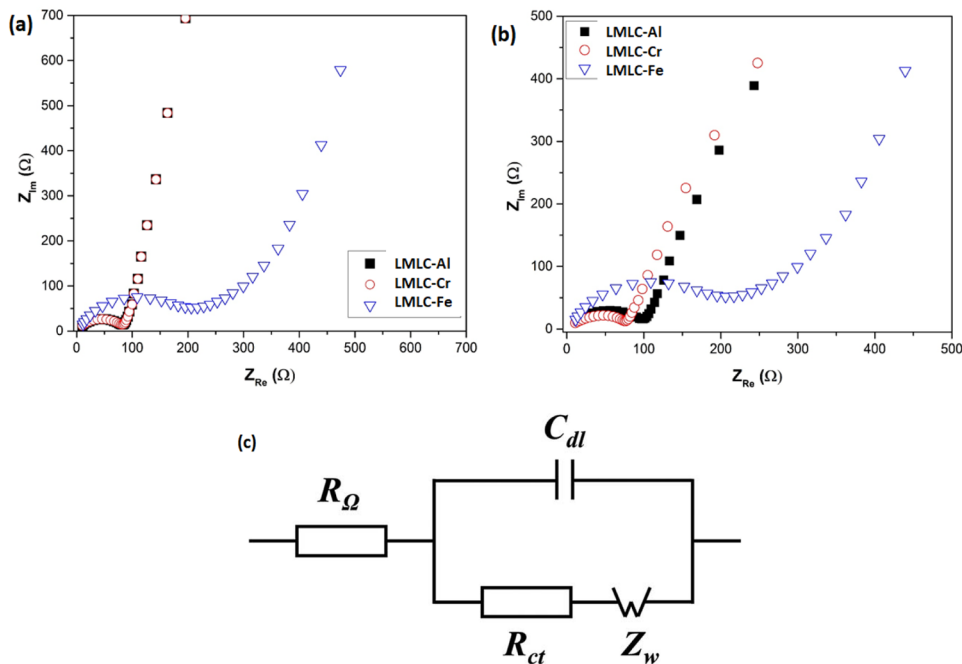


**Table 4** Electrochemical impedance spectroscopy fitting parameters for the LMLC cells before cycling and after 10th cycles

Electrode materials	$R_s$ ( $\Omega$ )		$R_{CT}$ ( $\Omega$ )		$Z_w$ ( $\Omega \cdot s^{0.5}$ )	
	Zero cycle	10th cycle	Zero cycle	10th cycle	Zero cycle	10th cycle
LMLC-Al	7.5	9.5	46.4	57.7	321	269.4
LMLC-Cr	7.8	10.3	26.1	39.9	236.8	216.9
LMLC-Fe	10.7	12.6	154.3	224.2	434.1	433.7

cell possesses the lowest resistance values for transport of charges ( $R_{ct}$ ) and lithium ions diffusion ( $Z_w$ ) before and after cycling as depicted in Table 4. In contrast to that, the LMLC-Fe cell reveals the maximum values for  $R_s$ ,  $R_{ct}$  and  $Z_w$  among the three cells before and after cycling that may lead to poor electrochemical performance upon cycling at different current rates or for large number of cycles. The reason for such behavior because LMLC-Fe sample has the lowest degree of transition elements occupation inside the Li-O layers and lowest amount of layered  $\text{Li}_2\text{MnO}_3$  structure of  $(\text{Li}[\text{Li}_{1/3}\text{Mn}_{2/3}]\text{O}_2)$  type as previously discussed in the XRD results.

### 3.4.3 Rate performance and cycle life

The electrode geometrical area was  $1.1 \text{ cm}^2$ ; the active mass loadings of LMLC-Al, LMLC-Cr or LMLC-Fe were 4.01, 3.67 and 4.93 mg, respectively, and the calculated theoretical capacities were as follows: 278.4, 277.46 and 277.63 mAh/g. The practical discharge capacities from selected test cells of the three cathode materials as a function of the C-rate are presented in Fig. 8. The coulombic efficiencies during the formation cycle were about 69, 60 and 50% for LMLC-Cr, LMLC-Al and LMLC-Fe, respectively. The low coulombic efficiency of the layered NCM electrodes is well described

in the literature [60–63]. However, a low initial coulombic efficiency after formation is not a necessary prerequisite for bad electrode performance, since it usually rises in the subsequent cycles, reaching 90–99%, as it was also in the case at hand.

In the initial cycle after formation, the mean discharge capacities at 0.1C were 104, 93 and 95 mAh/g for LMLC-Al, LMLC-Cr and LMLC-Fe cells, respectively. At 1 C the LMLC-Al and LMLC-Cr materials maintained around 70% of their initial capacity at 0.1C while the LMLC-Fe exhibited capacity fade down to ca. 60%. Generally, during the galvanostatic tests all the layered M-doped LMLC cathode materials showed around 65% lower capacities than the theoretically calculated and a relatively poor rate capability, particularly after 2C discharge rate (Fig. 8).

Figure 9 shows the subsequent long-term cycling (500 cycles) performances at 1C/2C of charge–discharge rate. During the long-term cycling the LMLC-Fe cathode showed the highest capacity decline down to zero, already after 360 cycles. This result is also in accordance with the measured EIS, where it was found that the cell with Fe-doped LMLC showed the maximum charge transfer resistance and a relatively poor  $\text{Li}^+$  ion diffusion between the electrolyte and electrode surface. The capacity of LMLC-Al after 500 cycles faded to 7% of the initial one, before the galvanostatic C-rate

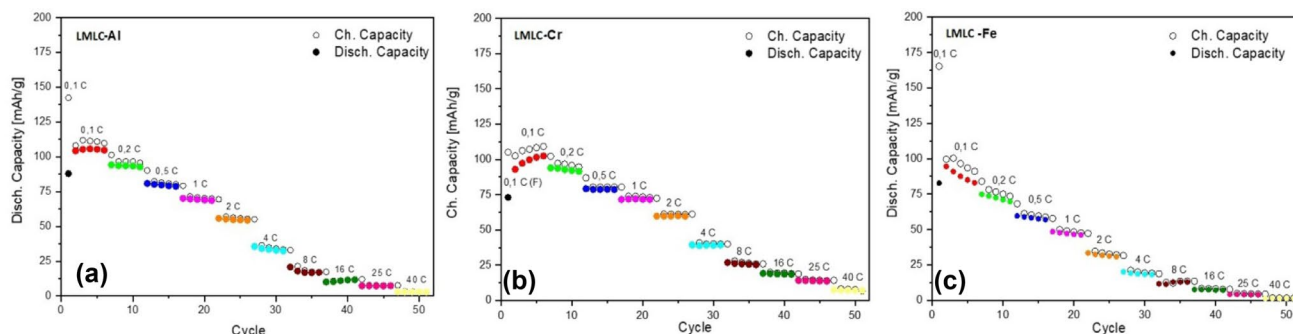


**Fig. 8** Rate capability tests with formation cycle: **a** LMLC-Al, **b** LMLC-Cr, and **c** LMLC-Fe

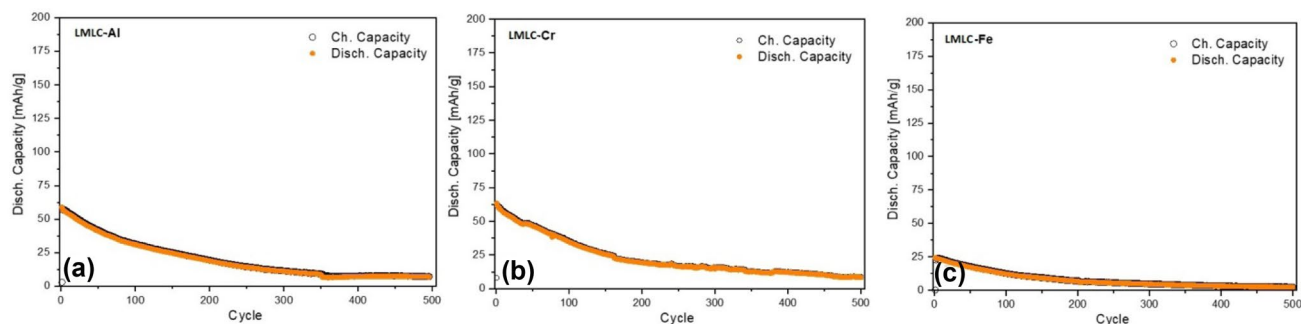


**Fig. 9** Long-term cycling tests **a** LMLC-Al, **b** LMLC-Cr and **c** LMLC-Fe at charge/discharge rate 1C/2C

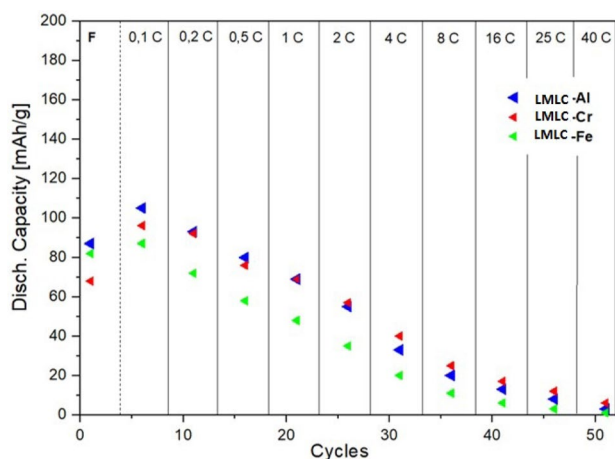


**Fig. 10** Mean discharge capacities at different C-rates for LMLC-Al, LMLC-Cr and LMLC-Fe cells. The letter *F* refers to the formation step or initial charge/discharge

tests. Meanwhile, the LMLC-Cr maintained approximately 10 mAh/g after 500 cycles, which corresponds to ca. 10% of the initial capacity before the C-rate testing.

According to the galvanostatic tests, the Al-doped LMLC cell exhibits the highest capacity after formation, until 0.1C. Thereafter, its capacity output mostly overlaps with those of LMLC-Cr up to 4 C and both materials perform generally better as the LMLC-Fe. The higher the C-rate, the less the capacity difference between the samples as displayed in Fig. 10. The compared results of mean discharge capacities at different C-rates are in a good agreement with CV and EIS measurements. The excellent storage capabilities of LMLC-Al at initial cycles and lower C-rates correspond to the highest occupation of Li–O layers in the  $\text{Li}_2\text{MnO}_3$  structure resulting in large extent of lithium ion extraction. The improved electrochemical behavior for LMLC-Cr cathode at higher C-rates could be assigned to the smallest crystallite/particle size and high electronic conductivity as well as the enhanced diffusion of lithium ions [64, 65].

## 4 Conclusions

The present study successfully employed the facile processing of three kinds of LMLC materials via solvothermal method. The as-prepared electrode materials were comparatively inspected for their crystal structure, chemical composition and microstructure through the advanced characterization techniques e.g. XRD, XPS, FE-SEM and HR-TEM. The results indicated that doping of LMLC with very small percentage of  $\text{Al}^{3+}$  causes significant increase in the crystallite size and cell volume which enable hosting larger extent of Li–O layers in the layered framework structure. Moreover, as Cr-doped LMLC material exhibited

the smallest particle size, it also demonstrated the best electronic and ionic conductivity. Although LMLC-Fe recorded the highest *H<sub>c</sub>* value, it also possessed the lowest *M<sub>s</sub>* and *M<sub>r</sub>* values. The Al-doped LMLC layered cathode indicated an improved electrochemical storage behavior during initial formation cycles due to the improved structure stability with good Li extraction giving rise in the electrolyte conductivity. The incorporation of 1%  $\text{Cr}^{3+}$  to the LMLC layered structure relatively improves the rate capability performance over 50 cycles and promotes the cyclability over subsequent 500 cycles. Nevertheless, Fe-doped layered LMLC showed the maximum charge transfer resistance and poor  $\text{Li}^+$  ion diffusion between the electrolyte and electrode surface.

**Supplementary Information** The online version contains supplementary material available at <https://doi.org/10.1007/s00339-021-04884-0>.

**Acknowledgements** The author is grateful and thankful to Science and Technology Development Fund (STDF) for the financial support of the work through German-Egyptian Research Fund (GERF) grant ID: 23038. Great thanks are extended to The Hydrogen and Fuel Cell Center–Duisburg (Germany) for performing the rate capability and long-term cycling test of batteries under the assistance and supervision of Dipl.-Ing. Bernd Oberschachtsiek and Dr. George Topalov at the department of electrolysis and batteries. Deep acknowledgments are presented to Dr. Sebastian Wennig (Hydrogen and Fuel Cell Center–Duisburg–Germany) for providing language and scientific help.

## Declarations

**Conflict of interest** The author declares that he has no conflict of interest.

## References

1. A.M. Gaikwad, B.V. Khau, G. Davies, B. Hertzberg, D.A. Steingart, A.C. Arias, A high areal capacity flexible lithium-ion battery with a strain-compliant design. *Adv. Energy Mater.* **5**, 1401389 (2015). <https://doi.org/10.1002/aenm.201401389>
2. M.S. Whittingham, Introduction: batteries. *Chem. Rev.* **114**, 11413–11413 (2014). <https://doi.org/10.1021/cr500639y>
3. Z. Lu, D.D. Macneil, J.R. Dahn, Layered cathode materials  $\text{Li}[\text{Nix}_{(2/3-x)/3}]_2\text{O}_2$  for lithium-ion batteries. *Electrochem. Solid-State Lett.* **34**, 191 (2001). <https://doi.org/10.1149/1.1407994>
4. M.M. Thackeray, S.H. Kang, C.S. Johnson, J.T. Vaughey, S.A. Hackney, Comments on the structural complexity of lithium-rich  $\text{Li}_{1+x}\text{M}_{1-x}\text{O}_2$  electrodes (M= Mn, Ni, Co) for lithium batteries. *Electrochem. Commun.* **8**, 1531–1538 (2006). <https://doi.org/10.1016/j.elecom.2006.06.030>
5. X.J. Guo, Y.X. Li, M. Zheng, J.M. Zheng, J. Li, Z.L. Gong, Y. Yang, Structural and electrochemical characterization of  $x\text{Li}[\text{Li}_{1/3}\text{Mn}_{2/3}\text{O}_2-(1-x)\text{Li}[\text{Ni}_{1/3}\text{Mn}_{1/3}\text{Co}_{1/3}]\text{O}_2$  ( $0 < x < 0.9$ ) as cathode materials for Li ion batteries. *J Power Sources* **184**, 414–419 (2008). <https://doi.org/10.1016/j.jpowsour.2008.04.013>
6. H. Yu, H. Kim, Y. Wang, P. He, D. Asakura, Y. Nakamura, H. Zhou, High-energy composite layered manganese-rich cathode materials via controlling  $\text{Li}_2\text{MnO}_3$  phase activation for lithium-ion batteries. *Phys. Chem. Chem. Phys.* **14**, 6584–6595 (2012). <https://doi.org/10.1039/C2CP40745K>

7. H. Pan, T. Zhu, S. Zhang, Y. Jiang, J. Chen, M. Gao, Y. Liu, Li- and Mn-rich layered oxide cathode materials for lithium-ion batteries: a review from fundamentals to research progress and applications. *Mol. Syst. Des. Eng.* **3**, 748–803 (2018). <https://doi.org/10.1039/c8me00025e>
8. A. Manthiram, J.C. Knight, S.-T. Myung, S.-M. Oh, Y.-K. Sun, M. Gu, I. Belharouak, Nickel-rich and lithium-rich layered oxide cathodes: progress and perspectives. *Adv. Energy Mater.* **6**, 1501010 (2016). <https://doi.org/10.1002/aenm.201501010>
9. X. Yang, X. Wang, Q. Wei, H. Shu, L. Liu, S. Yang, B. Hu, Y. Song, G. Zou, L. Hu, L. Yi, Synthesis and characterization of a Li-rich layered cathode material  $\text{Li}_{1.15}[(\text{Mn}_{1/3}\text{Ni}_{1/3}\text{Co}_{1/3})_{0.5}(\text{Ni}_{1/4}\text{Mn}_{3/4})_{0.5}]_{0.85}\text{O}_2$  with spherical core-shell structure. *J. Mater. Chem.* **22**, 19666–19672 (2012). <https://doi.org/10.1039/C2JM34259F>
10. H.J. Yu, H.S. Zhou, High-energy cathode materials ( $\text{Li}_2\text{MnO}_3$ - $\text{LiMO}_2$ ) for lithium-ion batteries. *J. Phys. Chem. Lett.* **4**, 1268–1280 (2013). <https://doi.org/10.1021/jz400032v>
11. X. Dong, Y.L. Xu, S. Yan, S.C. Mao, L.L. Xiong, X.F. Sun, Towards low-cost, high energy density  $\text{Li}_2\text{MnO}_3$  cathode materials. *J. Mater. Chem. A* **3**, 670–679 (2015). <https://doi.org/10.1039/C4TA02924K>
12. J.R. Croy, D. Kim, M. Balasubramanian, K. Gallagher, S.H. Kang, M.M. Thackeray, Countering the voltage decay in high capacity  $x\text{Li}_2\text{MnO}_3-(1-x)\text{LiMO}_2$  electrodes (M: Mn Ni, Co) for Li-ion batteries. *J. Electrochem. Soc.* **159**, A781–A790 (2012). <https://doi.org/10.1149/2.080206jes>
13. S. Yang, G. Huang, S. Hu, X. Hou, Y. Huang, M. Yue, G. Lei, Improved electrochemical performance of the  $\text{Li}_{1.2}\text{Ni}_{0.13}\text{Co}_{0.13}\text{Mn}_{0.54}\text{O}_2$  wired by CNT networks for Li-ion batteries. *Mater. Lett.* **118**, 8–11 (2014). <https://doi.org/10.1016/j.matlet.2013.11.071>
14. J.R. Croy, M. Balasubramanian, K.G. Gallagher, A.K. Burrell, Review of the U.S. Department of Energy’s “deep dive” to understand voltage fade in Li- and Mn-rich cathodes. *Acc. Chem. Res.* **48**, 2813–2821 (2015). <https://doi.org/10.1021/acs.accounts.5b00277>
15. A. Kumar, R. Nazzario, L. Torres-Castro, A. Pena-Duarte, M.S. Tomar, Electrochemical properties of MgO-coated 0.5  $\text{Li}_2\text{MnO}_3$ -0.5  $\text{LiNi}_0.5\text{Mn}_0.5\text{O}_2$  composite cathode material for lithium ion battery. *Int. J. Hydrog. Energy* **40**, 4931–4935 (2015)
16. L. Zhong, H. Jian-He, H. Gang, L. Lu, Effect of  $\text{FePO}_4$  coating on performance of  $\text{Li}_{1.2}\text{Mn}_{0.54}\text{Ni}_{0.13}\text{Co}_{0.13}\text{O}_2$  as cathode material for Li-ion battery. *J. Inorg. Mater.* **30**, 129–134 (2015)
17. S. Yamamoto, H. Noguchi, W.W. Zhao, Improvement of cycling performance in Ti substituted 0.5 $\text{Li}_2\text{MnO}_3$ -0.5 $\text{LiNi}_0.5\text{Mn}_0.5\text{O}_2$  through suppressing metal dissolution. *J. Power Sources* **278**, 76–86 (2015). <https://doi.org/10.1016/j.jpowsour.2014.12.038>
18. H. Chen, Q. Hu, Z. Huang, Z. He, Z. Wang, H. Guo, X. Li, Synthesis and electrochemical study of Zr-doped  $\text{Li}[\text{Li}_{0.2}\text{Mn}_{0.54}\text{Ni}_{0.13}\text{Co}_{0.13}]\text{O}_2$  as cathode material for Li-ion battery. *Ceram. Inter.* **42**, 263–269 (2016). <https://doi.org/10.1016/j.ceramint.2015.08.104>
19. Y. Zang, C. Ding, X. Wang, Z. Wen, C. Chen, Molybdenum-doped lithium-rich layered-structured cathode material  $\text{Li}_{1.2}\text{Ni}_{0.2}\text{Mn}_{0.6}\text{O}_2$  with high specific capacity and improved rate performance. *Electrochem. Acta* **168**, 234–239 (2015). <https://doi.org/10.1016/j.electacta.2015.03.223>
20. Z. He, Z. Wang, H. Guo, X. Li, P. Yue, J. Wang, X. Xiong, Synthesis and electrochemical performance of  $x\text{Li}_2\text{MnO}_3-(1-x)\text{LiMn}_0.5\text{Ni}_0.4\text{Co}_0.1\text{O}_2$  for lithium ion battery. *Powder Technol.* **235**, 158–162 (2013). <https://doi.org/10.1016/j.powtec.2012.09.020>
21. H. Xu, S. Deng, G. Chen, Improved electrochemical performance of  $\text{Li}_{1.2}\text{Mn}_{0.54}\text{Ni}_{0.13}\text{Co}_{0.13}\text{O}_2$  by Mg doping for lithium ion battery cathode material. *J. Mater. Chem.* **2**, 15015–15021 (2014). <https://doi.org/10.1039/C4TA01790K>
22. H. Li, H. Guo, Z. Wang, J. Wang, X. Li, N. Chen, W. Gui, Improving rate capability and decelerating voltage decay of Li-rich layered oxide cathodes by chromium doping. *Inter. Journal Hydr. Ener.* **43**, 11109–11119 (2018). <https://doi.org/10.1016/j.ijhydene.2018.04.203>
23. F. Nobili, F. Croce, R. Tossici, I. Meschini, P. Reale, R. Marassi, Sol-gel synthesis and electrochemical characterization of Mg-/Zr-doped  $\text{LiCoO}_2$  cathodes for Li-ion batteries. *J. Power Sources* **197**, 276–284 (2012). <https://doi.org/10.1016/j.jpowsour.2011.09.053>
24. L. Croguennec, J. Bains, J. Bréger, C. Tessier, P. Biensan, S. Levasseur, C. Delmas, Effect of aluminum substitution on the structure, electrochemical performance and thermal stability of  $\text{Li}_{1+x}(\text{Ni}_{0.40}\text{Mn}_{0.40}\text{Co}_{0.20-z}\text{Al}_z)_{1-x}\text{O}_2$ . *J. Electrochem. Soc.* **158**, A664–A670 (2011). <https://doi.org/10.1149/1.3571479>
25. C. Lu, S. Yang, H. Wu, Y. Zhang, X. Yang, T. Liang, Enhanced electrochemical performance of Li-rich  $\text{Li}_{1.2}\text{Mn}_{0.52}\text{Co}_{0.08}\text{Ni}_{0.2}\text{O}_2$  cathode materials for Li-ion batteries by vanadium doping. *Electrochem. Acta* **209**, 448–455 (2016). <https://doi.org/10.1016/j.electacta.2016.05.119>
26. X. Feng, Y. Gao, L. Ben, Z. Yang, Z. Wang, L. Chen, Enhanced electrochemical performance of Ti-doped  $\text{Li}_{1.2}\text{Mn}_{0.54}\text{Co}_{0.13}\text{Ni}_{0.13}\text{O}_2$  for lithium-ion batteries. *J. Power Sources* **317**, 74–80 (2016). <https://doi.org/10.1016/j.jpowsour.2016.03.101>
27. Y. Zhao, G. Sun, R. Wu, Synthesis of nanosized Fe-Mn based Li-rich cathode materials for lithium-ion battery via a simple method. *Electrochim. Acta* **96**, 291–297 (2013). <https://doi.org/10.1016/j.electacta.2013.01.059>
28. Q.-Q. Qiao, L. Qin, G.-R. Li, Y.-L. Wang, X.-P. Gao, Sn-stabilized Li-rich layered  $\text{Li}(\text{Li}_{0.17}\text{Ni}_{0.23}\text{Mn}_{0.58})\text{O}_2$  oxide as a cathode for advanced lithium-ion batteries. *J. Mater. Chem. A* **3**, 17627–17634 (2015). <https://doi.org/10.1039/C5TA03415A>
29. C.-C. Wang, Y.-C. Lin, P.-H. Chou, Mitigation of layer to spinel conversion of a lithium-rich layered oxide cathode by substitution of Al in a lithium ion battery. *RSC Adv.* **5**, 68919–68928 (2015). <https://doi.org/10.1039/C5RA11665A>
30. P.K. Nayak, J. Grinblat, M. Levi, E. Levi, S. Kim, J.W. Choi, D. Aurbach, Al doping for mitigating the capacity fading and voltage decay of layered Li and Mn-rich cathodes for Li-ion batteries. *Adv. Energy Mater.* (2016). <https://doi.org/10.1002/aenm.201502398>
31. P.K. Nayak, J. Grinblat, E. Levi, M. Levi, B. Markovsky, D. Aurbach, Understanding the influence of Mg doping for the stabilization of capacity and higher discharge voltage of Li- and Mn-rich cathodes for Li-ion batteries. *Phys. Chem. Chem. Phys.* **19**, 6142–6152 (2017). <https://doi.org/10.1039/C6CP07383B>
32. Y.-J. Kang, J.-H. Kim, S.-W. Lee, Y.-K. Sun, The effect of  $\text{Al}(\text{OH})_3$  coating on the  $\text{Li}[\text{Li}_{0.2}\text{Ni}_{0.2}\text{Mn}_{0.6}]\text{O}_2$  cathode material for lithium secondary battery. *Electrochem. Acta* **50**, 4784–4791 (2005). <https://doi.org/10.1016/j.electacta.2005.02.032>
33. T. Zhao, S. Chen, L. Li, X. Zhang, R. Chen, I. Belharouak, F. Wu, K. , Amine, Synthesis, characterization, and electrochemistry of cathode material  $\text{Li}[\text{Li}_{0.2}\text{Co}_{0.13}\text{Ni}_{0.13}\text{Mn}_{0.54}]\text{O}_2$  using organic chelating agents for lithium-ion batteries. *J. Power Sources* **228**, 206–213 (2013). <https://doi.org/10.1016/j.jpowsour.2012.11.099>
34. F. Fu, Y.Y. Huang, P. Wu, Y.K. Bu, Y.B. Wang, J.N. Yao, Controlled synthesis of lithium-rich layered  $\text{Li}_{1.2}\text{Mn}_{0.56}\text{Ni}_{0.12}\text{Co}_{0.12}\text{O}_2$  oxide with tunable morphology and structure as cathode material for lithium-ion batteries by solvo/hydrothermal methods. *J. Alloys Compd.* **618**, 673–678 (2015). <https://doi.org/10.1016/j.jallcom.2014.08.191>
35. E. Markevich, G. Salitra, Y. Talyosef, U.-H. Kim, H.-H. Ryu, Y.-K. Sun, D. Aurbach, High performance  $\text{LiNiO}_2$  cathodes with

- practical loading cycled with Li metal anodes in fluoroethylene carbonate based electrolyte solution. *ACS Appl. Energy Mater.* **1**, 2600–2607 (2018). <https://doi.org/10.1021/acsaem.8b00304>
36. A. Boulineau, L. Croguennec, C. Delmas, F. Weill, Structure of  $\text{Li}_2\text{MnO}_3$  with different degrees of defects. *Solid State Ionics* **180**, 1652–1659 (2010). <https://doi.org/10.1016/j.ssi.2009.10.020>
  37. S. Alagar, C.-C. Yang, C. Karupiah, R. Madhuvilakku, S. Piraman, Temperature-controlled synthesis of Li- and Mn-Rich  $\text{Li}_{1.2}\text{Mn}_{0.54}\text{Ni}_{0.13}\text{Co}_{0.13}\text{O}_2$  hollow nano/sub-microsphere electrodes for high-performance lithium-ion battery. *ACS Omega* **4**(23), 20285–20296 (2019). <https://doi.org/10.1021/acsomega.9b02766>
  38. B. Seteni, N. Rapulenyane, J.C. Ngila, H. Luo, Structural and electrochemical behavior of  $\text{Li}_{1.2}\text{Mn}_{0.54}\text{Ni}_{0.13}\text{Co}_{0.13-x}\text{Al}_x\text{O}_2$  ( $x = 0.05$ ) positive electrode material for lithium ion battery. *Mater Today Proc* **5**, 10479–10487 (2018). <https://doi.org/10.1016/j.matpr.2017.12.379>
  39. S. Rajarathinam, S. Mitra, R.K. Petla,  $\text{Li}_2\text{MnO}_3$  rich- $\text{LiMn}_{0.33}\text{Co}_{0.33}\text{Ni}_{0.33}\text{O}_2$  integrated nano-composites as high energy density lithium-ion battery cathode materials. *Electrochem. Acta* **108**, 135–144 (2013). <https://doi.org/10.1016/j.electacta.2013.06.102>
  40. D. Mohanty, A.S. Sefat, S. Kalnaus, J. Li, R.A. Meisner, E.A. Payzant, D.P. Abraham, D.L. Wood, C. Daniel, Investigating phase transformation in the  $\text{Li}_{1.2}\text{Co}_{0.1}\text{Mn}_{0.55}\text{Ni}_{0.15}\text{O}_2$  lithium-ion battery cathode during high-voltage hold (4.5 V) via magnetic, X-ray diffraction and electron microscopy studies. *J. Mater. Chem. A* **1**, 6249–6261 (2013). <https://doi.org/10.1039/C3TA10304H>
  41. Q. Xia, D.G. Ivey, X. Zhao, M. Xu, W. Wei, Z. Ding, J. Liu, L. Chen, A Li-rich layered@spinel@carbon heterostructured cathode material for high capacity and high rate lithium-ion batteries fabricated via an in situ synchronous carbonization-reduction method. *J. Mater. Chem. A* **3**, 3995–4003 (2015). <https://doi.org/10.1039/C4TA05848H>
  42. Y. Tian, M. Chen, S. Xue, Y. Cai, Q. Huang, X. Liu, W. Li, Template-determined microstructure and electrochemical performances of li-rich layered metal oxide cathode. *J. Power Sources* **401**, 343–353 (2018). <https://doi.org/10.1016/j.jpowsour.2018.09.010>
  43. K. Amine, H. Tukamoto, H. Yasuda, Y. Fujita, A new three-volt spinel  $\text{Li}_{1+x}\text{Mn}_{1.5}\text{Ni}_{0.5}\text{O}_4$  for secondary lithium batteries. *J. Electrochem. Soc.* **143**, 1607–1613 (1996). <https://doi.org/10.1149/1.1836686>
  44. K.M. Shaju, R.G.V. Subbu, B.V.R. Chowdari, Performance of layered  $\text{LiNi}_{1/3}\text{Co}_{1/3}\text{Mn}_{1/3}\text{O}_2$  as cathode for Li-ion batteries. *Electrochim. Acta* **48**, 145–151 (2002). [https://doi.org/10.1016/S0013-4686\(02\)00593-5](https://doi.org/10.1016/S0013-4686(02)00593-5)
  45. J. Huang, X. Fang, Y. Wu, L. Zhou, Y. Wang, Y. Jin, W. Dang, L. Wu, Z. Rong, X. Chen, X. Tang, Enhanced electrochemical performance of  $\text{LiNi}_{0.8}\text{Co}_{0.1}\text{Mn}_{0.1}\text{O}_2$  by surface modification with lithium-active  $\text{MoO}_3$ . *J. Electroanal. Chem.* **823**, 359–367 (2018)
  46. Y. Zhao, M. Xia, X. Hu, Z. Zhao, Y. Wang, Z. Lv, Effects of Sn doping on the structural and electrochemical properties of  $\text{Li}_{1.2}\text{Ni}_{0.2}\text{Mn}_{0.8}\text{O}_2$  Li-rich cathode materials. *Electrochim. Acta* **174**, 1167–1174 (2015). <https://doi.org/10.1016/j.electacta.2015.05.068>
  47. Z. Chen, J. Wang, D.L. Chao, T. Baikie, L. Bai, S. Chen, Y. Zhao, T.C. Sum, J. Lin, Z. Shen, Hierarchical porous  $\text{LiNi}_{1/3}\text{Co}_{1/3}\text{Mn}_{1/3}\text{O}_2$  nano-/micro spherical cathode material: minimized cation mixing and improved  $\text{Li}^+$  mobility for enhanced electrochemical Performance. *Sci. Rep.* **6**, 25771 (2016). <https://doi.org/10.1038/srep25771>
  48. J. Hong, K. Kang, H. Gwon, S.K. Jung, K. Ku, Review—Lithium- excesslayered cathodes for lithium rechargeable batteries. *J. Electrochem. Soc.* **162**, A2447–A2467 (2015). <https://doi.org/10.1149/2.0071514jes>
  49. H. Pan, S. Zhang, J. Chen, M. Gao, Y. Liu, T. Zhu, Y. Jiang, Li- and Mn-rich layered oxide cathode materials for lithium-ion batteries: a review from fundamentals to research progress and applications. *Mol. Syst. Des. Eng.* **3**, 748–803 (2018). <https://doi.org/10.1039/C8ME00025E>
  50. N.A. Chernova, M. Ma, J. Xiao, M.S. Whittingham, J.C. Jiménez, C.P. Grey, Magnetic studies of layered cathode materials for lithium ion batteries. *Mater. Res. Soc. Symp. Proc.* **972**, 610 (2007). <https://doi.org/10.1557/PROC-0972-AA06-10>
  51. N.A. Chernova, M. Ma, M. Jie Xiao, Stanley Whittingham, Julien Breger, Clare P. Grey, Layered  $\text{Li}_x\text{Ni}_y\text{Mn}_z\text{Co}_{1-2y}\text{O}_2$  cathodes for lithium ion batteries: understanding local structure via magnetic properties. *Chem. Mater.* **19**, 482–4693 (2007). <https://doi.org/10.1021/cm0708867>
  52. M.N. Ates, S. Mukerjee, K.M. Abraham, A high rate Li-rich layered MNC cathode material for lithium-ion batteries. *RSC Adv.* **5**, 27375–27386 (2015). <https://doi.org/10.1039/C4RA17235C>
  53. Y. Errami, M. Ouassaid, M. Cherkaoui, M. Maaroufi, Maximum power point tracking control based on a nonlinear back stepping approach for a permanent magnet synchronous generator wind energy conversion system connected to a utility grid. *Ener. Technol.* **3**, 743–757 (2015). <https://doi.org/10.1002/ente.201500026>
  54. D. Harbaoui, M.M.S. Sanad, C. Rossignol, E. Hlil, N. Amdouni, S. Obbade, Synthesis and structural, electrical, and magnetic properties of new iron–aluminum alluaudite phases  $\beta\text{-Na}_2\text{Ni}_2\text{M}(\text{PO}_4)_3$  ( $\text{M} = \text{Fe}$  and  $\text{Al}$ ). *Inorg. Chem.* **56**, 13051–13061 (2017). <https://doi.org/10.1021/acs.inorgchem.7b01880>
  55. N. Murali, K.V. Babu, K.E. Babu, V. Veeraiah, Structural and conductivity studies of  $\text{LiNi}_{0.5}\text{Mn}_{0.5}\text{O}_2$  cathode materials for lithium-ion batteries. *Mater. Sci-Pol.* **34**, 404–411 (2016)
  56. N. Murali, V. Veeraiah, Preparation, dielectric and conductivity studies of  $\text{LiNi}_{1-x}\text{Mg}_x\text{O}_2$  cathode materials for lithium-ion batteries. *Process. Appl. Ceram.* **11**, 258–264 (2017). <https://doi.org/10.2298/PAC1704258M>
  57. N. Murali, S.J. Margarete, V. Veeraiah, Synthesis, dielectric, conductivity and magnetic studies of  $\text{LiNi}_{1/3}\text{Co}_{1/3}\text{Mn}_{1/3-x}\text{Al}_x\text{O}_2$  ( $x=0.0, 0.02, 0.04$  and  $0.06$ ) for cathode materials of lithium-ion batteries. *Results Phys.* **7**, 1379–1388 (2017). <https://doi.org/10.1016/j.rinp.2017.02.037>
  58. H. Arai, S. Okada, Y. Sakurai, J.-I. Yamaki, Reversibility of  $\text{LiNiO}_2$  cathode. *Solid State Ionics* **95**, 275–282 (1997). [https://doi.org/10.1016/S0167-2738\(96\)00598-X](https://doi.org/10.1016/S0167-2738(96)00598-X)
  59. S.S. Zhang, K. Xu, T.R. Jow, Formation of solid electrolyte interface in lithium nickel mixed oxide electrodes during the first cycling. *Electrochem. Solid-State Lett.* **5**, A92–A94 (2002). <https://doi.org/10.1149/1.1464506>
  60. J.P. Peres, C. Delmas, A. Rougier, M. Broussely, F. Perton, P. Biensan, P. Willmann, The relationship between the composition of lithium nickel oxide and the loss of reversibility during the first cycle. *J. Phys. Chem. Solids* **57**, 1057–1060 (1996). [https://doi.org/10.1016/0022-3697\(95\)00395-9](https://doi.org/10.1016/0022-3697(95)00395-9)
  61. C. Delmas, J.P. Peres, A. Rougier, A. Demourgues, F. Weill, A. Chadwick, M. Broussely, F. Perton, P. Biensan, P. Willmann, On the behavior of  $\text{Li}_x\text{NiO}_2$  system: an electrochemical and structural overview. *J. Power Sources* **68**, 120–125 (1997). [https://doi.org/10.1016/S0378-7753\(97\)02664-5](https://doi.org/10.1016/S0378-7753(97)02664-5)
  62. J.R. Mueller-Neuhaus, R.A. Dunlap, J.R. Dahn, Understanding irreversible capacity in  $\text{Li}_x\text{Ni}_{1-y}\text{Fe}_y\text{O}_2$  cathode materials. *J. Electrochem. Soc.* **147**, 3598–3605 (2000)
  63. J. Choi, A. Manthiram, Investigation of the irreversible capacity loss in the layered  $\text{LiCo}_{1/3}\text{Ni}_{1/3}\text{Mn}_{1/3}\text{O}_2$  cathodes. *Electrochem. Solid-State Lett.* **8**, C102–C105 (2005). <https://doi.org/10.1149/1.1943567>
  64. A.Y. Shenouda, M.M.S. Sanad, Synthesis, characterization and electrochemical performance of  $\text{Li}_2\text{Ni}_x\text{Fe}_{1-x}\text{SiO}_4$  cathode

- materials for lithium ion batteries. *Bull. Mater. Sci.* **40**, 1055–1060 (2017). <https://doi.org/10.1007/s12034-017-1449-2>
65. A. Abdel-Aziz, A.Y. Shenouda, M.M.S. Sanad, B. Kishore, H.F.Y. Khalil, M.M.B. El-Sabbah, Effect of ionic substitutions on the physicochemical, morphological, and electrochemical properties of lithium-rich vanadium phosphate and pyrophosphate compounds. *Ionics* **25**, 969–980 (2019). <https://doi.org/10.1007/s11581-019-02843-7>

**Publisher's Note** Springer Nature remains neutral with regard to jurisdictional claims in published maps and institutional affiliations.